

# Thick Lunar Crust Amplifies Gravitational-Wave Signal

Lei Zhang<sup>1</sup> <sup>\*</sup> Han Yan<sup>2,3</sup> <sup>\*</sup> Xian Chen<sup>2,3</sup> <sup>†</sup> and Jinhai Zhang<sup>1</sup> <sup>‡</sup>

<sup>1</sup>*Institute of Geology and Geophysics, Chinese Academy of Sciences, Beijing 100029, China*

<sup>2</sup>*Department of Astronomy, School of Physics, Peking University, 100871 Beijing, China* and

<sup>3</sup>*Kavli Institute for Astronomy and Astrophysics, Peking University, 100871 Beijing, China*

(Dated: January 26, 2026)

Gravitational waves (GWs) in the  $10^{-3} - 0.1$  Hz band encode unique signatures of the early universe and merging compact objects, but they are beyond the reach of existing observatories. Theoretical models suggest that the Moon could act as a resonant detector, but the unknown influence of its rugged surface and heterogeneous interior has cast doubt on this prospect. Here, we resolve this long-standing uncertainty by constructing the first high-resolution, structurally realistic model of the lunar GW response. We achieve this by combining high-fidelity spectral-element simulations with the analytical power of normal-mode perturbation theory, thereby resolving topographical effects down to 3.7 km grid spacing while maintaining the capacity to discern global free-oscillation patterns. This dual-methodology approach not only recovers the expected predominant quadrupole ( $l = 2$ ) oscillation mode, but also exposes a systematic signal amplification of (10 – 20)% in thick-crust regions. This enhancement is traced by our normal-mode analysis to a mode-coupling process, in which the original quadrupolar oscillation induced by the passing GWs distributes energy into a series of higher-order modes, the hybridized eigenmodes of the laterally heterogeneous Moon. Near certain eigen-frequencies and at specific locations, we observe up to tenfold amplification, highlighting the power of numerical simulations in resolving these structurally fine-tuned features. Our work establishes the Moon as an accurately calibrated resonant GW detector, and the resulting amplification maps provide quantitative guide for the optimal landing site selection.

*Introduction.*—Gravitational waves (GWs) have been observed in the hundred-hertz band by ground-based interferometers [1–4] and in the nano-hertz band by pulsar timing arrays [5–8]. In between lies the mid band ( $10^{-3} - 0.1$  Hz) where many intriguing sources exist, including the seeds of supermassive black holes, inspiraling binary stellar black holes or neutron stars, supernovae, as well as quantum fluctuations in the early universe [9, 10]. The detection of these sources defines the core science cases for future space-based GW detectors like LISA, TianQin, Taiji [10–12], and other projects [13, 14].

An alternative proposal of detecting mid-band GWs is to find a celestial body which can act as a giant resonant detector [15–17]. In this spirit, the Moon offers a unique platform due to its quietness compared to the Earth [18]. Assuming spherical symmetry, earlier analytical works established that only the Moon’s quadrupole ( $l = 2$ ) mode resonates with GW [19, 20], and the resonant peaks lie in the mid band [19, 21–23]. These one-dimension models also revealed the importance of lunar radial structure in determining the resonant frequencies [23, 24].

In reality, the Moon is *not* a spherically symmetric body but has strong variations in both topography and crustal thickness, since altimetric surveys indicate tens of kilometers in topographic relief [25, 26] and lunar gravity measurements reveal strong lateral variations in crustal thickness [27, 28]. Many studies based on normal-mode perturbation theory [29, 30] show that strong lat-

eral velocity variations would severely impact the resonance of seismic wave propagation within the Earth, especially for the normal mode coupling and energy redistribution [31–33]. However, the effect of such heterogeneity on the GW response of the Earth and the Moon remains unknown. If not properly understood, it may mislead our conclusion for lunar GW detection [34]. This issue is becoming even more pressing for the proposed projects like Lunar Gravitational-Wave Antenna (LGWA) [35, 36], Gravitational-wave Lunar Observatory for Cosmology (GLOC) [37], Laser Interferometer Lunar Antenna (LILA) [38], and other lunar GW projects [39–41].

Using conventional normal-mode perturbation analysis [29, 30] to address this issue presents distinct advantages and limitations. A major advantage arises from the simplicity of the GW source term: unlike earthquakes or moonquakes, which excite a broad spectrum of seismic modes, GWs interact almost exclusively with the Moon’s quadrupole ( $l = 2$ ) modes, drastically simplifying the analytical description. However, this approach becomes computationally demanding when accounting for the full mode-mixing induced by lateral heterogeneities, and it struggles to provide a fine-scale description of the resulting surface displacement field. To complement the perturbation analysis, in the past few years we have developed high-fidelity numerical simulations based on the high-order finite-element (FEM), specifically the spectral-element method (SEM) [42, 43], which enables precise modeling of wave propagation across realistic lunar topography [44–46]. Although computationally intensive, the SEM provides a direct numerical testbed for verifying key analytical predictions, particularly in re-

<sup>\*</sup> The first two authors contributed equally to this work.

<sup>†</sup> Contacting author: xian.chen@pku.edu.cn

<sup>‡</sup> Contact author: zjh@mail.igcas.ac.cn

gions of strong topographic and crustal variations. However, 3D simulations remain computationally prohibitive for long-duration GW signals. Therefore, it is essential to develop a novel calculation framework that combines the high resolution of the FEM method and the generality of the normal-mode analysis to reveal both the fine details of the lunar response and the underlying physical mechanism.

For the above reason, we present the first structurally realistic model of the lunar GW response: high-precision two-dimensional (2D) SEM simulations employed to resolve the effects of rugged topography and strong non-uniform crustal structures, while a three-dimensional (3D) mode-coupling approach characterizes the global low-order response. Our results show that the Moon's crustal asymmetry acts as a potent amplifier, efficiently redistributing energy from the GW-excited quadrupole modes into a rich spectrum of higher-order spheroidal modes. This mode-mixing process not only enhances signal detectability in specific frequency bands but also indicates the potential of GW-induced seismic responses to constrain the Moon's 3D internal structure.

*Numerical simulation of lunar response to GWs.*—We first perform 2D numerical simulations to quantify how lunar topography and crustal structure modulate the GW-induced surface displacement and velocity fields. Details of modeling and parameter setting can be found in Supplemental Material. Our lunar model integrates topographic and crustal-thickness data from the LOLA [25] and GRAIL [26] missions, incorporating major structural features such as the South Pole–Aitken (SPA) basin, Mare Imbrium, and Mare Humboldtianum (Figure 1). From it we extract the topographic and crustal profiles along a selected great circle and map them directly into a 2D model. Dyson-type force density is applied to model the GW sources [17]. Our model achieves a maximum resolved frequency of 0.2 Hz with time-step constrained to 0.035 s, ensuring both numerical stability and computational tractability. Then we use the SEM [42] to simulate the excitation of seismic activity by GWs and the 2D propagation of seismic waves. We focus on the response in the frequency band of 0.001–0.2 Hz. Figure 2(a–d) shows that the lateral heterogeneity of structures has significant impact on the lunar response to GWs. Compared with the results obtained by spherically layered models [22, 42], the wavefronts in the realistic model are distorted, especially in Mare Imbrium, Mare Humboldtianum, and the SPA basin.

To quantify the impact of lunar topography and crustal thickness variation, we define an amplification factor  $M_E$  as the ratio of local displacement energy ( $|\vec{s}(\vec{r}, \omega)|^2$ ) with or without lateral heterogeneity (marked with “P” or “NP”), integrated over frequency:

$$M_E(\vec{r}) = \frac{\int_{\omega_{\min}}^{\omega_{\max}} \langle |\vec{s}^P(\vec{r}, \omega)|^2 \rangle_{\text{pol}} d\omega}{\int_{\omega_{\min}}^{\omega_{\max}} \langle |\vec{s}^{\text{NP}}(\vec{r}, \omega)|^2 \rangle_{\text{pol}} d\omega} . \quad (1)$$

Here,  $\langle \rangle_{\text{pol}}$  denotes an average over all polarization, in order to separate the amplification due to lunar structure

from polarization-induced variations in the GW amplitude. More details of this equation are discussed in the Supplemental Material.

Figure 2e presents the distribution of  $M_E$  along a typical great circle. The spatial characteristics generally show strong correlations with both topography and crustal thickness. Notably, thick-crust regions (e.g., highlands) show an average signal amplification (red curve in Figure 2e). However, in some places such as Mare Imbrium, where the topography has almost no relief, the amplification ratios still vary dramatically with the varying crustal thickness. This key observation demonstrates that crustal thickness rather than topography is the dominant factor of governing the amplification effect. Hence, we should pay more attention to the crustal thickness when evaluating lunar local response to GWs.

To find the optimal frequency band for GW search, we plot the frequency-dependent amplification ratio  $m_E(\omega)$ , defined as

$$m_E(\vec{r}, \omega) = \frac{\langle |\vec{s}^P(\vec{r}, \omega)|^2 \rangle_{\text{pol}}}{\langle |\vec{s}^{\text{NP}}(\vec{r}, \omega)|^2 \rangle_{\text{pol}}} , \quad (2)$$

in Figure 2f, where we have applied a median-filter smoothing to reveal fundamental patterns. The plot shows that the amplification is prominent in the 1.5–30 mHz band and there are rich spectral peaks with bandwidths as narrow as  $\sim 0.05$  mHz. The peaks appear on the highlands surrounding the SPA basin, coinciding with the thickest crust (refer to Figure 1c). For example, on the highland between  $\varphi = 70^\circ$  and  $120^\circ$ ,  $m_E(\omega)$  can reach tenfold. Moreover, the peak frequencies align closely with the resonant frequencies of the lunar response function [42], suggesting a direct link to the normal modes of the Moon.

*Normal mode perturbation method.*—The observed close correspondence between crust thickness and GW signal amplification in our numerical simulations can be understood in the theoretical framework of normal-mode perturbation and mixing. In the ideal case where the Moon is spherically symmetric, non-rotating, elastic, and isotropic (SNREI), its free oscillation can be described by a series of orthonormal normal modes  $|k\rangle \equiv |\sigma, n, l, m\rangle$  which are eigenfunctions of the secular equation

$$\mathcal{V}|k\rangle = \omega_k^2 \mathcal{T}|k\rangle \quad (3)$$

[30]. Here,  $\mathcal{V}$  and  $\mathcal{T}$  are potential and kinetic operators, respectively. The presence of surface topography and crustal variation perturbs the operators by  $\delta\mathcal{V}$  and  $\delta\mathcal{T}$ , restructuring the eigenmodes. Given that the perturbation is small, the new modes can be approximated by a linear combination of the basic SNREI modes, so that

$$|i\rangle = \sum_k C_{ki} |k\rangle . \quad (4)$$

For this reason, the new modes are also known as the “hybridized modes”. The transformation matrix  $\mathbf{C}$  sat-

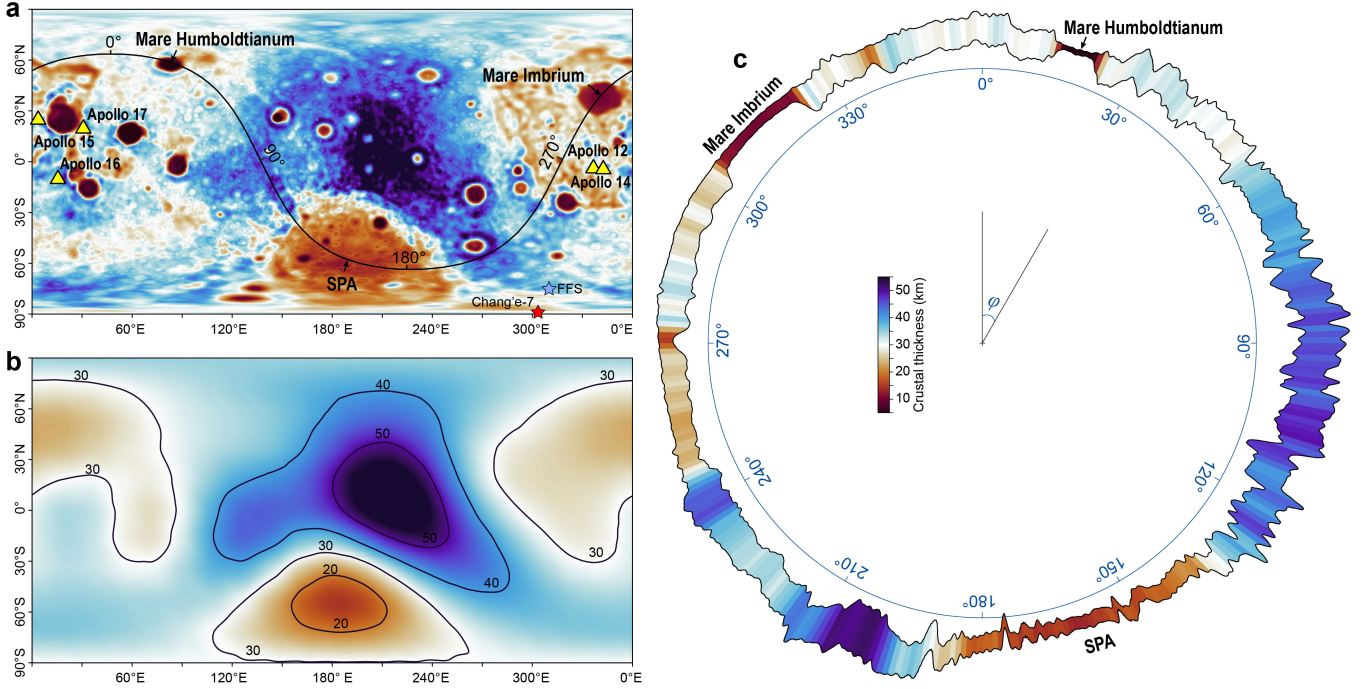


FIG. 1. Lunar model with topography and crustal-thickness variations. (a) Lunar crustal thickness model. The yellow triangles mark the locations of Apollo seismographs. The black line indicates the great circle passing through Mare Humboldtianum, Mare Imbrium, and the SPA basin. The potential landing sites of Chang'e-7 and FFS are marked as stars around the south pole. (b) Crustal thickness model truncated at  $l = 4$ . Solid lines represent crustal thickness contours in km. (c) The topography and crustal thickness along the great circle shown in (a), magnified by 30 and 5 times, respectively, to reveal details.

isfies the perturbed equation

$$\sum_{k'} (\omega_k^2 \delta_{kk'} + V_{kk'}) C_{k'i} = \Omega_i^2 \sum_{k'} (\delta_{kk'} + T_{kk'}) C_{k'i} \quad (5)$$

[33], where  $\Omega_i$  denotes the perturbed eigenfrequency,  $V_{kk'} = \langle k | \delta \mathcal{V} | k' \rangle$  and  $T_{kk'} = \langle k | \delta \mathcal{T} | k' \rangle$  are the elements of the coupling matrices which can be calculated using Woodhouse kernels [29].

GWs exert a tidal force  $\vec{f}_{\text{GW}}$  on the Moon. Owing to their quadrupole character, this force couples almost exclusively to the unperturbed  $l = 2$  modes. In a laterally heterogeneous Moon, however, these unperturbed SNREI modes are no longer the true eigenmodes. Instead, they hybridize according to Equation (4). Consequently, the energy initially in the quadrupole modes is systematically redistributed into the hybridized mode spectrum. This mode mixing process is captured by the following equation,

$$\vec{s}^{\mathcal{P}}(\vec{r}, \omega) = \sum_i \frac{\langle \vec{r} | i \rangle \langle i | \vec{f}_{\text{GW}} \rangle}{\Omega_i^2 - \omega^2} = \sum_i \frac{\sum_k C_{ki} \vec{u}_k(\vec{r})}{\Omega_i^2 - \omega^2} \left( \sum_{k' \in \{\sigma_l=S2\}} C_{k'i}^* f_{k'} \right) \quad (6)$$

where  $\vec{s}^{\mathcal{P}}(\vec{r}, \omega)$  is the seismic displacement field at location  $\vec{r}$ ,  $\vec{u}_k(\vec{r})$  is the unperturbed free-oscillation pattern,

and  $f_{k'}$  is the projection of the GW force onto the unperturbed mode  $|k'\rangle$ . The detailed derivation of this core equation can be found in the Supplemental Material.

We implement this framework using the topography model derived from NASA's GRAIL Model 2 data [26], which is already visualized in Fig. 1(a). For comparison, the one-dimension SNREI model is adopted from our previous work with slight modification [47]. To maintain computational tractability while preserving key large-scale asymmetries, notably the farside–nearside dichotomy, we truncate the spherical-harmonic expansion of the Moon at  $l_{\text{max}} = 4$ , yielding the approximate lunar model shown in Fig. 1(b). In the hybridized mode calculation, we allow free-oscillation modes up to  $l = 6$  and  $n = 100$ , reflecting both the selection rule and numerical feasibility. Toroidal modes are excluded because GW couples predominantly to spheroidal modes, and toroidal eigenfunctions exhibit lower accuracy in standard solvers such as MINEOS [48].

Fig. 3(a) shows the band-integrated total magnification  $M_E(\vec{r})$  across the lunar surface. This map reveals a robust and systematic pattern, with values deviating from unity by approximately  $(10 - 20)\%$ , consistent with the crustal-thickness dependence observed in our 2D numerical simulations. This spatial pattern exhibits a clear correlation with the underlying crustal structure shown in Fig. 1(b): regions of thin crust, such as the nearside maria, consistently exhibit de-amplification ( $M_E < 1$ ),

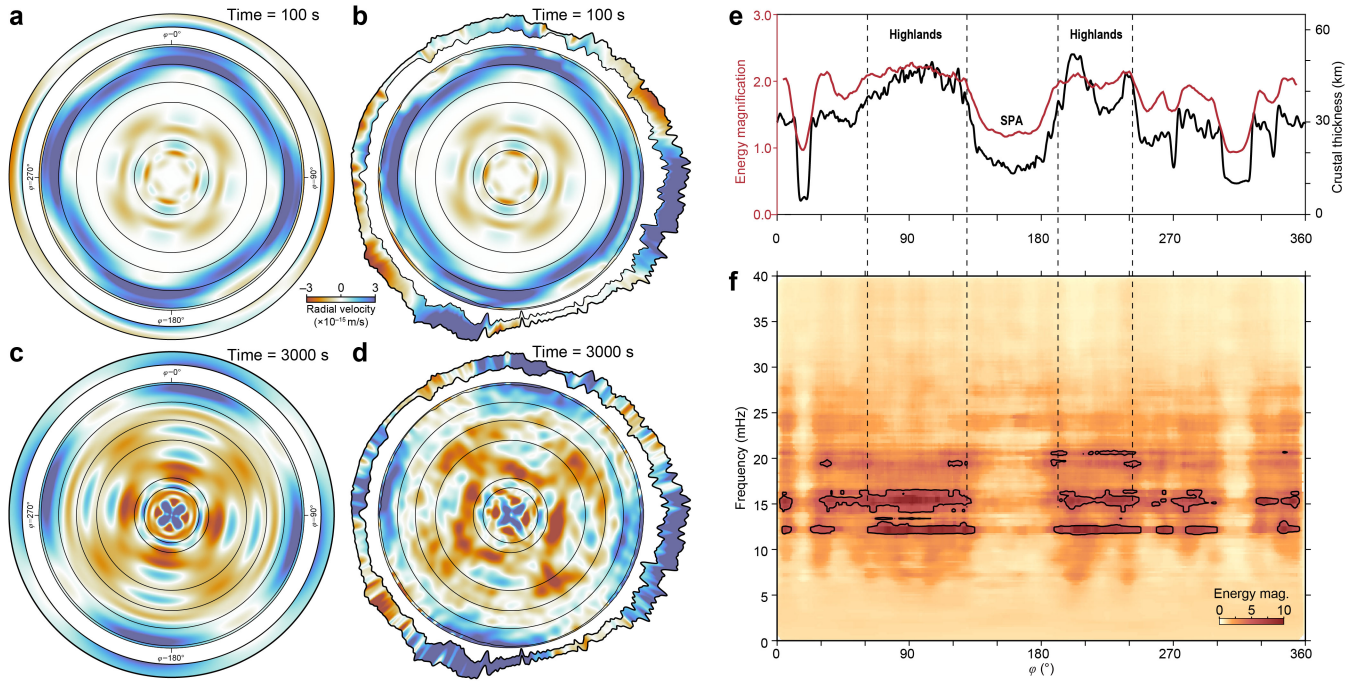


FIG. 2. Comparison between layered and heterogeneous models and the simulated location-frequency distribution of amplification ratios. (a) The snapshot of lunar response to GWs for a spherically layered model at  $t = 100$  s. (b) The same as (a) but for the model with varying topography and crustal thickness shown in Figure 1c. In a and b, the topography and crustal thickness are magnified by 30 and 5 times in the outside annulus, respectively. (c) The same as (a) but at  $t = 3000$  s. (d) The same as (b) but at  $t = 3000$  s. More snapshots can be found in [47]. (e) The averaged amplification ratio  $M_E$  (red line). The black line is the crustal thickness for reference. (f) The amplification ratio  $m_E(\omega)$  of the vertical component in the frequency band 0–40 mHz, where the black contour lines indicate the amplification ratio of 5.

whereas the thick-crust terrains of the farside highlands show pronounced amplification. This correlation confirms the role of crustal thickness in modulating the Moon’s global seismic response to GWs. It also points to a direct link between lateral heterogeneity and surface observables.

To more clearly trace the cause of the amplification, Fig. 3(b) isolates the contribution to  $M_E$  from the fundamental quadrupole mode  $\vec{u}_{l=2}$  alone. The resulting map shows values near unity, with much smaller variation ( $\sim 4\%$ ) and weaker correlation to crustal thickness. This result implies that the amplification pattern seen in Fig. 3(a) is not primarily due to modulation of the  $l = 2$  mode, but rather emerges from the collective response of higher-order modes ( $l > 2$ ) excited through mode mixing.

*Discussions and implications.*—In this Letter, we have elucidated how the rugged surface and heterogeneous crust of the Moon can modulate the surface seismic signals triggered by GWs. We achieve this by developing a calculation framework which combines the advantages of two complementary approaches: a perturbation theory provides an efficient and transparent physical picture of global mode mixing, whereas the SEM delivers the high spatial resolution required to capture complex local wavefield distortions at the expense of greater computational cost.

Our SEM simulation not only recovers the GW-induced quadrupole mode of the lunar free oscillation but also reveals a close link of the seismic amplitude to the crustal thickness. On average, the seismic signal can be amplified by (10 – 20)% in thick-crust regions. Near the normal-mode frequencies of 15 and 20 mHz, the amplification can exceed one order of magnitude. These findings establish a direct link between crustal structure and GW detectability. Regions characterized by thicker crust, particularly the farside highlands, consistently exhibit an amplification of the GW signal, therefore offer better opportunities for GW detection.

Our simulations also pinpoint the strongest signal amplification in a couple of frequency bands that can be as narrow as 0.05 mHz. Resolving such narrow features requires long-duration, low-noise observations since a bandwidth of 0.05 mHz implies a minimum observational period of  $T \sim 1/(0.05 \text{ mHz}) \approx 2 \times 10^4 \text{ s} \approx 6 \text{ h}$ . Therefore, continuous seismic data collection spanning one day or longer is recommended.

The correlation between signal amplification and crust thickness is also verified by our analytical normal-mode perturbation model. The analysis further identifies mode mixing as the origin of the enhancement: The Moon’s crustal asymmetry reshapes its eigenmodes, enabling the energy from a purely quadrupolar perturbation—such as

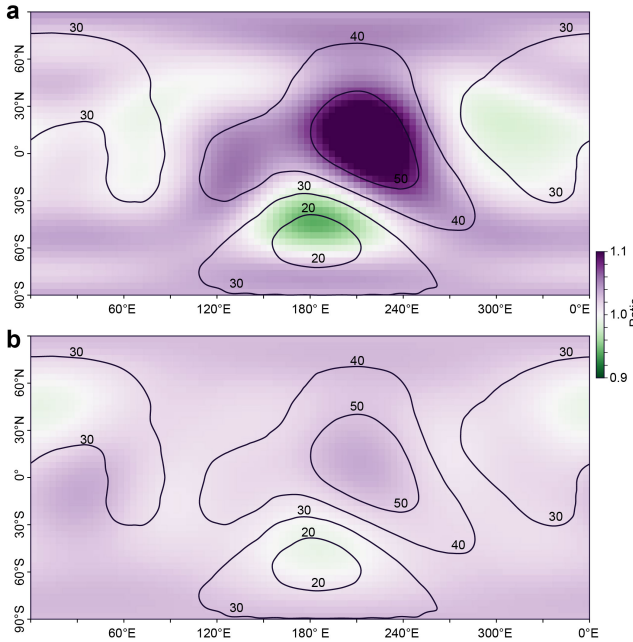


FIG. 3. Amplification according to the normal-mode perturbation theory. (a) Total energy magnification  $M_E$ , integrated over frequency and averaged over polarization. Here, all the free-oscillation modes up to  $l = 6$  are included. (b) Contribution from the  $l = 2$  free-oscillation mode alone. For comparison, the crustal thickness contours from Fig. 1(b) are overlaid.

that imposed by a passing GW—to transfer into an ensemble of higher-order free-oscillation modes. Such a correlated, structured signal across the lunar surface differs fundamentally from the stochastic, spatially incoherent background of seismic noise. By employing a matched-filter correlation approach (e.g., see Refs [22] and [49]) that incorporates our theoretical model of the hybridized modes, we can in principle statistically separate the GW-induced seismic response from the spectrally and spatially diffuse lunar seismic background.

Several caveats are worth mentioning. Our numerical (SEM) simulations here were restricted to 2D by computational cost. The mode-coupling calculation excluded toroidal modes and was also truncated at relatively low spherical harmonic degrees. Future work should bridge these gaps by performing full 3D SEM simulations and extending the mode-coupling basis set to higher  $l_{\max}$  for cross-validation. Furthermore, while this work focuses on

polarization-averaged effects to reveal global structural correlations, specific GW events (single incident direction and polarization) may exhibit even sharper local amplifications due to the constructive interference between the global quadrupolar driving force and the local structural heterogeneity. Modeling and understanding these complex, event-specific interactions will be crucial for precise source parameter estimation in future GW observations.

Finally, we emphasize that the integration of global mode-coupling theory with high-resolution SEM simulations provides the framework necessary to calibrate the Moon as a resonant GW antenna. Beyond enabling the detection of mid-band GW sources, this approach also works reciprocally. In principle, observed GW signals could be analyzed to constrain the Moon's 3D internal structure, complementing traditional seismic surveys. This interdependence hints at a promising future for lunar GW seismology as a dual-purpose diagnostic tool.

## ACKNOWLEDGMENTS

This work is supported by the National Natural Science Foundation of China (NSFC) Grants No. 42325406, and the National Key Research and Development Program of China Grant No. 2024YFC2207300. Han Yan acknowledges support from the China Scholarship Council (No. 202506010256), and thanks Gran Sasso Science Institute for hospitality during the manuscript revision. The authors would like to thank many people for helpful discussions: Jan Harms for various ideas about lunar detection, Li Zhao and Yanbin Wang for mode-coupling theory, and Zhaorong Fu for matrix computations.

J. Zhang and X. Chen conceived and designed the research. L. Zhang performed the numerical SEM simulations and amplification analysis. H. Yan developed the theoretical mode-coupling framework and conducted the semi-analytical calculations. L. Zhang and H. Yan contributed equally to the data analysis and drafted the manuscript. All authors contributed to the interpretation of results and the revision of the paper.

The elevation data is derived from Lunar Orbiter Laser Altimeter (LOLA, <https://pds-geosciences.wustl.edu/missions/lro/lola.htm>). The lunar crustal thickness model is derived from <https://github.com/MarkWieczorek/ctplanet>.

- 
- [1] B. P. Abbott, R. Abbott, T. D. Abbott, et al., Observation of Gravitational Waves from a Binary Black Hole Merger, *Phys. Rev. Lett.* **116**, 061102 (2016), arXiv:1602.03837 [gr-qc].
- [2] A. Abramovici, W. E. Althouse, et al., LIGO: The Laser Interferometer Gravitational-Wave Observatory, *Science* **256**, 325 (1992).
- [3] F. Acernese, M. Agathos, et al., Advanced Virgo: a second-generation interferometric gravitational wave detector, *Classical and Quantum Gravity* **32**, 024001 (2015), arXiv:1408.3978 [gr-qc].
- [4] Kagra Collaboration, T. Akutsu, M. Ando, et al., KAGRA: 2.5 generation interferometric gravitational wave detector, *Nature Astronomy* **3**, 35 (2019),

- arXiv:1811.08079 [gr-qc].
- [5] H. Xu, S. Chen, Y. Guo, et al., Searching for the Nano-Hertz Stochastic Gravitational Wave Background with the Chinese Pulsar Timing Array Data Release I, *Research in Astronomy and Astrophysics* **23**, 075024 (2023), arXiv:2306.16216 [astro-ph.HE].
- [6] EPTA Collaboration, InPTA Collaboration, et al., The second data release from the European Pulsar Timing Array. III. Search for gravitational wave signals, *Astronomy & Astrophysics* **678**, A50 (2023), arXiv:2306.16214 [astro-ph.HE].
- [7] G. Agazie, M. F. Alam, A. Anumarpudi, et al., The NANOGrav 15 yr Data Set: Observations and Timing of 68 Millisecond Pulsars, *The Astrophysical Journal Letters* **951**, L9 (2023), arXiv:2306.16217 [astro-ph.HE].
- [8] D. J. Reardon, A. Zic, R. M. Shannon, et al., Search for an Isotropic Gravitational-wave Background with the Parkes Pulsar Timing Array, *The Astrophysical Journal Letters* **951**, L6 (2023), arXiv:2306.16215 [astro-ph.HE].
- [9] M. Arca Sedda, C. P. L. Berry, K. Jani, et al., The missing link in gravitational-wave astronomy: discoveries waiting in the decihertz range, *Classical and Quantum Gravity* **37**, 215011 (2020), arXiv:1908.11375 [gr-qc].
- [10] M. Colpi, K. Danzmann, et al., LISA Definition Study Report, arXiv e-prints , arXiv:2402.07571 (2024), arXiv:2402.07571 [astro-ph.CO].
- [11] J. Luo, L.-S. Chen, H.-Z. Duan, et al., TianQin: a space-borne gravitational wave detector, *Classical and Quantum Gravity* **33**, 035010 (2016), arXiv:1512.02076 [astro-ph.IM].
- [12] Z. Luo, Y. Wang, Y. Wu, W. Hu, and G. Jin, The Taiji program: A concise overview, *Progress of Theoretical and Experimental Physics* **2021**, 05A108 (2021).
- [13] S. Kawamura, M. Ando, N. Seto, et al., The Japanese space gravitational wave antenna: DECIGO, *Classical and Quantum Gravity* **28**, 094011 (2011).
- [14] W.-T. Ni, Core noise and GW sensitivities of AMIGO, *International Journal of Modern Physics D* **31**, 2250039 (2022), arXiv:2106.12432 [gr-qc].
- [15] J. Weber, Detection and Generation of Gravitational Waves, *Physical Review* **117**, 306 (1960).
- [16] J. Weber, Gravitational Waves, *Physics Today* **21**, 34 (1968).
- [17] F. J. Dyson, Seismic Response of the Earth to a Gravitational Wave in the 1-Hz Band, *Astrophys. J.* **156**, 529 (1969).
- [18] P. Lognonné, M. Le Feuvre, C. L. Johnson, and R. C. Weber, Moon meteoritic seismic hum: Steady state prediction, *Journal of Geophysical Research (Planets)* **114**, E12003 (2009).
- [19] A. Ben-Menahem, Excitation of the earth's eigen vibrations by gravitational radiation from astrophysical sources., *Nuovo Cimento C Geophysics Space Physics* **C 6**, 49 (1983).
- [20] M. Bianchi, E. Coccia, C. N. Colacino, V. Fafone, and F. Fucito, Testing theories of gravity with a spherical gravitational wave detector, *Classical and Quantum Gravity* **13**, 2865 (1996), arXiv:gr-qc/9604026 [gr-qc].
- [21] J. Majstorović, S. Rosat, and Y. Rogister, Earth's spheroidal motion induced by a gravitational wave in flat spacetime, *Phys. Rev. D* **100**, 044048 (2019).
- [22] H. Yan, X. Chen, J. Zhang, F. Zhang, M. Wang, and L. Shao, Toward a consistent calculation of the lunar response to gravitational waves, *Phys. Rev. D* **109**, 064092 (2024).
- [23] J. Majstorović, L. Vidal, and P. Lognonné, Modeling lunar response to gravitational waves using normal-mode approach and tidal forcing, *Phys. Rev. D* **111**, 044061 (2025), arXiv:2411.09559 [gr-qc].
- [24] X. Bi and J. Harms, Response of the Moon to gravitational waves, *Phys. Rev. D* **110**, 064025 (2024), arXiv:2403.05118 [gr-qc].
- [25] D. E. Smith, M. T. Zuber, et al., Initial observations from the Lunar Orbiter Laser Altimeter (LOLA), *Geophysical Research Letters* **37**, L18204 (2010).
- [26] M. A. Wieczorek, G. A. Neumann, F. Nimmo, et al., The Crust of the Moon as Seen by GRAIL, *Science* **339**, 671 (2013).
- [27] Y. H. Huang, J. M. Soderblom, D. A. Minton, M. Hirabayashi, and H. J. Melosh, Bombardment history of the moon constrained by crustal porosity, *Nature Geoscience* **15**, 531 (2022).
- [28] M. A. Wieczorek and R. J. Phillips, Potential anomalies on a sphere: Applications to the thickness of the lunar crust, *Journal of Geophysical Research: Planets* **103**, 1715 (1998).
- [29] J. H. Woodhouse, The coupling and attenuation of nearly resonant multiplets in the Earth's free oscillation spectrum, *Geophysical Journal* **61**, 261 (1980).
- [30] F. A. Dahlen and J. Tromp, *Theoretical Global Seismology* (Princeton University Press, 1999).
- [31] J. H. Woodhouse and F. A. Dahlen, The effect of a general aspherical perturbation on the free oscillations of the earth., *Geophysical Journal International* **53**, 335 (1978).
- [32] G. Masters, J. Park, and F. Gilbert, Observations of coupled spheroidal and toroidal modes, *Journal of Geophysical Research* **88**, 10285 (1983).
- [33] A. Deuss and J. H. Woodhouse, Theoretical free-oscillation spectra: the importance of wide band coupling, *Geophysical Journal International* **146**, 833 (2001).
- [34] X. Chen, The moon as a gateway to discovery: how lunar gravitational-wave detection advances science across disciplines, *npj Space Exploration* **2** (2026).
- [35] J. Harms, F. Ambrosino, L. Angelini, et al., Lunar Gravitational-wave Antenna, *Astrophys. J.* **910**, 1 (2021), arXiv:2010.13726 [gr-qc].
- [36] M. Branchesi, M. Falanga, J. Harms, et al., Lunar Gravitational-Wave Detection, *Space Science Reviews* **219**, 67 (2023).
- [37] K. Jani and A. Loeb, Gravitational-wave lunar observatory for cosmology, *Journal of Cosmology and Astroparticle Physics* **2021** (06), 044.
- [38] K. Jani, M. Abernathy, E. Berti, et al., Laser Interferometer Lunar Antenna (LILA): Advancing the U.S. Priorities in Gravitational-wave and Lunar Science, arXiv e-prints , arXiv:2508.11631 (2025), arXiv:2508.11631 [gr-qc].
- [39] H. J. Paik and K. Y. Venkateswara, Gravitational wave detection on the Moon and the moons of Mars, *Advances in Space Research* **43**, 167 (2009).
- [40] P. Amaro-Seoane, L. Bischof, J. J. Carter, M.-S. Hartig, and D. Wilken, LION: laser interferometer on the moon, *Classical and Quantum Gravity* **38**, 125008 (2021), arXiv:2012.10443 [astro-ph.IM].
- [41] J. Li, F. Liu, Y. Pan, Z. Wang, M. Cao, M. Wang, F. Zhang, J. Zhang, and Z.-H. Zhu, Detecting gravitational wave with an interferometric seismometer array

- on lunar nearside, *Science China Physics, Mechanics, and Astronomy* **66**, 109513 (2023).
- [42] L. Zhang, H. Yan, X. Chen, and J. Zhang, 2D numerical simulation of lunar response to gravitational waves using finite element method, *Phys. Rev. D* **111**, 063014 (2025), arXiv:2412.17898 [astro-ph.EP].
- [43] L. Zhang, H. Yan, J. Zhang, and X. Chen, Numerical simulation of lunar response to gravitational waves and its 3d topographic effect using the spectral-element method (2025), arXiv:2512.21667 [astro-ph.EP].
- [44] D. Komatitsch, S. Tsuboi, J. Tromp, A. Levander, and G. Nolet, The spectral-element method in seismology, *Geophysical Monograph-American Geophysical Union* **157**, 205 (2005).
- [45] L. Zhang, J. Wang, Y. Xu, C. He, and C. Zhang, A procedure for 3D seismic simulation from rupture to structures by coupling SEM and FEM, *Bulletin of the Seismological Society of America* **110**, 1134 (2020).
- [46] L. Zhang, H. Yan, J. Zhang, and X. Chen, Numerical simulation of lunar response to gravitational waves and its 3D topographic effect using the spectral-element method, arXiv e-prints , arXiv:2512.21667 (2025), arXiv:2512.21667 [astro-ph.EP].
- [47] See *CrustalAmplify* folder in <https://github.com/StrelitziaHY/LunarResponse> (2025).
- [48] G. Masters, J. H. Woodhouse, and G. Freeman, Mineos v1.0.2 [software], Computational Infrastructure for Geodynamics (2011), <https://geodynamics.org/cig>.
- [49] H. Yan, X. Chen, J. Zhang, F. Zhang, L. Shao, and M. Wang, Constraining the stochastic gravitational wave background using the future lunar seismometers, *Phys. Rev. D* **110**, 043009 (2024), arXiv:2405.12640 [gr-qc].
- [50] D. Komatitsch and J. Tromp, Spectral-element simulations of global seismic wave propagation—i. validation, *Geophysical Journal International* **149**, 390 (2002).
- [51] D. Komatitsch, J. Ritsema, and J. Tromp, The spectral-element method, beowulf computing, and global seismology, *Science* **298**, 1737 (2002).
- [52] L. Zhang, J. Zhang, and R. N. Mitchell, Dichotomy in crustal melting on early mars inferred from antipodal effect, *The Innovation* **3** (2022).

## SUPPLEMENTAL MATERIAL

### A. Numerical simulation using the spectral-element method

We use a finite-element SEM based on the code SPECFEM2D [50, 51] to calculate the lunar response to GWs. This method was originally proposed by Zhang et al. (2025) [42] to simulate the Earth seismic waves. In this work, we build a global 2D model of the Moon composed of over 140 thousand spectral elements with four control points on each element [42, 52]. Our model includes the great-circle profile of a 3D lunar model (Figure 1a), covering topographical features such as the center of the Mare Imbrium ( $40^\circ$  N,  $342^\circ$  E), the approximate center of the SPA ( $59^\circ$  S,  $193^\circ$  E), and the center of the Moon. For comparison, we also build a spherically layered model. For both models, the grid size is approximately 3.7 km in the horizontal direction on the ground surface, and it increases with the P-wave velocities. Receivers are arranged along the surface by an interval of  $1^\circ$ . Our model achieves a maximum resolved frequency of 0.2 Hz with time-step constrained to 0.035 s, ensuring both numerical stability and computational tractability.

### B. GW source modeling in the SEM simulation

To calculate the lunar response to GWs, we use the Dyson-type force density  $\vec{f}$  [22, 42]

$$\vec{f}_{\text{GW}} = \nabla \mu \cdot \mathbf{h}, \quad (\text{A1})$$

where  $\mathbf{h}$  refers to the spatial components of the GW tensor and  $\mu$  is the shear modulus. This force appears only in the layers with significant radial variation of the shear modulus, as shown in Figure A1d. To simulate the cases with different GW polarizations, we consider different polarization angles  $\theta = 0^\circ, 10^\circ, 20^\circ, \dots, 80^\circ$ , as shown in Figure A2. The source time function (STF) is a Gaussian wavelet with a dominant frequency of 20 mHz (Figure A1e,f). The entire simulation duration is 5000 s, which allows several rounds of seismic wave propagation through the Moon. The wall-clock time consumption is about 0.5 hours using 192 nodes with 12,288 cores on the cluster of the National Supercomputing Center in Wuxi, China.

### C. Secular Equation and Numerical Implementation

In our normal-mode analysis, the response of the Moon to GW is determined by solving the perturbed secular equation. As stated in the main text, this takes the form of a generalized eigenvalue problem:

$$[\text{Diag}(\omega_k^2) + \mathbf{V}] \mathbf{C} = \Omega^2 (\mathbf{I} + \mathbf{T}) \mathbf{C}, \quad (\text{A2})$$

where  $|k\rangle \equiv |\sigma, n, l, m\rangle$  denotes an unperturbed normal mode with eigenfrequency  $\omega_k$ .  $\mathbf{V}$  and  $\mathbf{T}$  are coupling matrices representing the perturbation's effect on potential and kinetic energy, respectively.  $\Omega_i$  and the columns of  $\mathbf{C}$  are the eigenfrequencies and eigenvectors of the perturbed system.

While Eq. (A2) is physically transparent, standard numerical eigensolvers are optimized for the standard form  $\mathbf{Ax} = \lambda \mathbf{x}$ . To adapt our problem, we rearrange Eq. (A2). A direct approach would be to compute  $(\mathbf{I} + \mathbf{T})^{-1}$  and left-multiply it, yielding:

$$(\mathbf{I} + \mathbf{T})^{-1} [\text{Diag}(\omega_k^2) + \mathbf{V}] \mathbf{C} = \Omega^2 \mathbf{C}. \quad (\text{A3})$$

However, the matrix  $\mathbf{T}$  is typically small for realistic planetary models. In our practical computation, we make a first-order approximation  $(\mathbf{I} + \mathbf{T})^{-1} \approx \mathbf{I} - \mathbf{T}$ . This adjustment moves the kinetic perturbation term to the left-hand side, resulting in a standard eigenvalue problem that is more computationally tractable:

$$(\mathbf{I} - \mathbf{T}) [\text{Diag}(\omega_k^2) + \mathbf{V}] \mathbf{C} \approx \Omega^2 \mathbf{C}. \quad (\text{A4})$$

This formulation enables us to efficiently include a large number of modes in the basis set.

It is worth noting that while near-degenerate perturbation theory offers a powerful analytical tool for understanding strong coupling between specific modes with close frequencies, it was not employed in our final calculation. Instead, we opted to solve the full matrix equation, approximated by Eq. (A4) directly. This method inherently includes coupling effects between all modes in the basis, thus avoiding the complexities of identifying near-degenerate pairs or potential divergences in the perturbative expansion [33].

### D. Gravitational Wave Forcing and Polarization

The seismic force exerted by a plane gravitational wave is quadrupolar in nature. The response of the Moon depends on the GW's propagation direction, polarization angle, as well as frequency. The effective force projected onto an unperturbed spheroidal mode  $|k'\rangle = |S, n', 2, m'\rangle$  is given by  $f_{k'} = \langle k' | \vec{f}_{\text{GW}} \rangle$ . This term can be separated into a GW amplitude  $h_0(\omega)$ , a radial integral dependent on the Moon's SNREI structure, and a geometric term dependent on the GW properties [21]:

$$f_{k'}(e, \lambda, \nu) = h_0 I_{n'} f_{m'}^{\text{geom}}(e, \lambda, \nu). \quad (\text{A5})$$

Three angles  $e, \lambda, \nu$  are commonly used to describe the propagation direction and polarization of GW [21]. The radial integral  $I_{n'}$  depends on the shear modulus profile  $\mu(r)$  and the radial eigenfunctions  $U_{n'2}(r)$  and  $V_{n'2}(r)$  of the unperturbed mode:

$$I_{n'} = \int_0^R \frac{\partial \mu}{\partial r} \left[ U_{n'2}(r) + \frac{3}{\sqrt{6}} V_{n'2}(r) \right] r^2 dr. \quad (\text{A6})$$

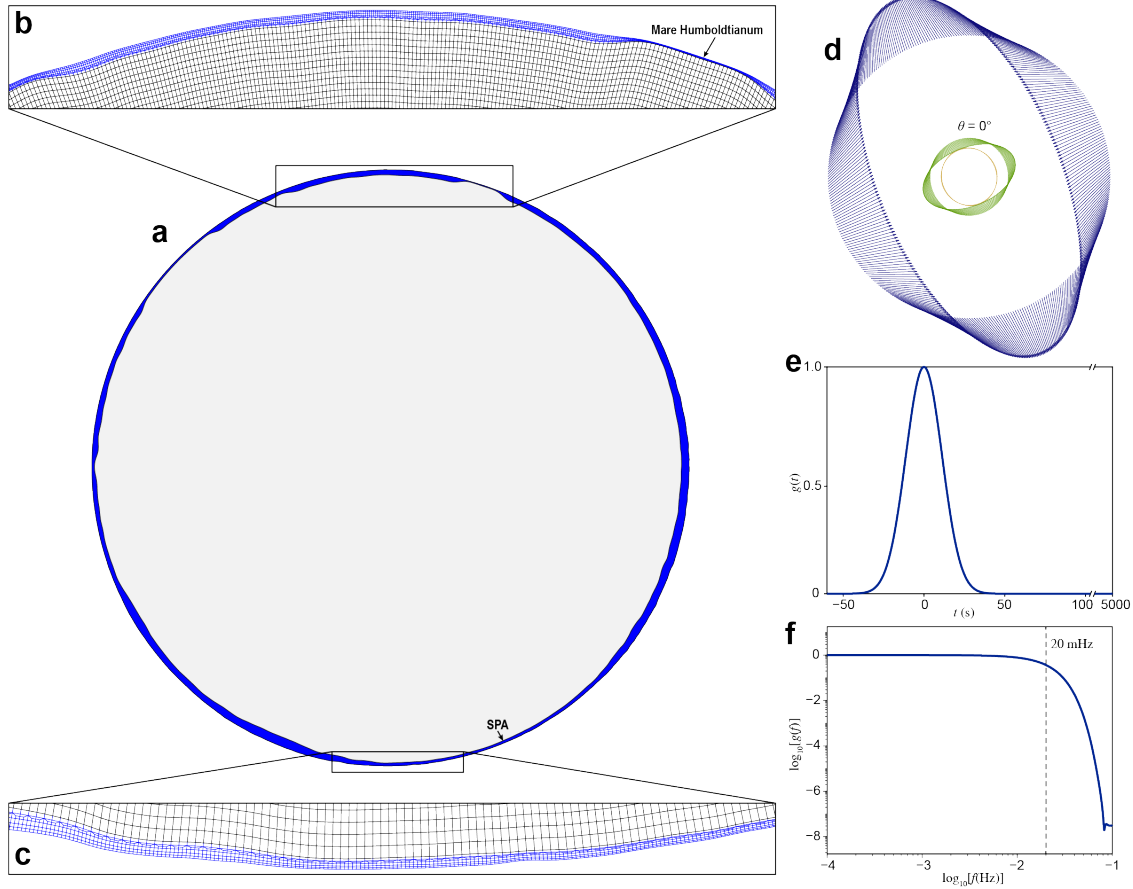


FIG. A1. The SEM grids and the GW-source model. (a) Global lunar model featuring crustal thickness variation, with a surface element size of about 3.7 km. (b) Enlarged regional crust grids around the azimuth of  $0^\circ$ . (c) Enlarged regional crust grids around the south pole. (d) Spatial distribution of the force density. (e) The source time function with a duration of 5,000 s. (f) The normalized amplitude spectrum.

The geometric term  $f_{m'}^{\text{geom}}$ , which we denote as  $f_{m'}$ , describes the antenna pattern of the mode. It depends on the GW's propagation direction, defined by ecliptic latitude  $e$  and longitude  $\lambda$ , and polarization angle  $\nu$ . Normally, the GW polarization tensor  $\epsilon$  is defined by two basis tensors  $\mathbf{e}^+$  and  $\mathbf{e}^\times$ :

$$\begin{aligned}\mathbf{e}^+ &= \hat{\mathbf{l}} \otimes \hat{\mathbf{l}} - \hat{\mathbf{m}} \otimes \hat{\mathbf{m}} \\ \mathbf{e}^\times &= \hat{\mathbf{l}} \otimes \hat{\mathbf{m}} + \hat{\mathbf{m}} \otimes \hat{\mathbf{l}}\end{aligned}\quad (\text{A7})$$

where the polarization basis vectors  $(\hat{\mathbf{l}}, \hat{\mathbf{m}})$  are orthogonal to the propagation direction  $\hat{\mathbf{k}}$ :

$$\begin{aligned}\hat{\mathbf{k}} &= (\sin e \cos \lambda, \sin e \sin \lambda, \cos e) \\ \hat{\mathbf{l}} &= (\cos e \cos \lambda, \cos e \sin \lambda, -\sin e) \\ \hat{\mathbf{m}} &= (-\sin \lambda, \cos \lambda, 0)\end{aligned}\quad (\text{A8})$$

The antenna pattern function  $f_{m'}(e, \lambda, \nu)$  for the five degenerate  $l = 2$  modes ( $m' \in \{-2, -1, 0, 1, 2\}$ ) is then

given by

$$\begin{aligned}f^m(e, \lambda, \nu) = & \frac{2}{3} \sqrt{\frac{\pi}{5}} \delta_{m,0} b_1 \sin^2 e \\ & + \delta_{m,2} \frac{C}{2} [4b_2 \cos e \cos 2\lambda + b_1 (3 + \cos 2e) \sin 2\lambda] \\ & + \delta_{m,-2} C [b_1 \cos 2\lambda (\cos^2 e + 1) - 2b_2 \cos e \sin 2\lambda] \\ & + \delta_{m,1} 2C \sin e [b_2 \cos \lambda + b_1 \cos e \sin \lambda] \\ & - \delta_{m,-1} 2C \sin e [b_2 \sin \lambda - b_1 \cos e \cos \lambda]\end{aligned}\quad (\text{A9})$$

[21], in which  $C = 2\sqrt{\pi/15}$ , and the coefficients  $b_1$  and  $b_2$  depend on the polarization angle  $\nu$ :

$$\begin{aligned}b_1 &= \cos(2\nu) - \sin(2\nu) \\ b_2 &= \cos(2\nu) + \sin(2\nu)\end{aligned}\quad (\text{A10})$$

## E. Polarization Averaging

To obtain a map for seismic amplification that is independent of a specific GW event, we average the seismic

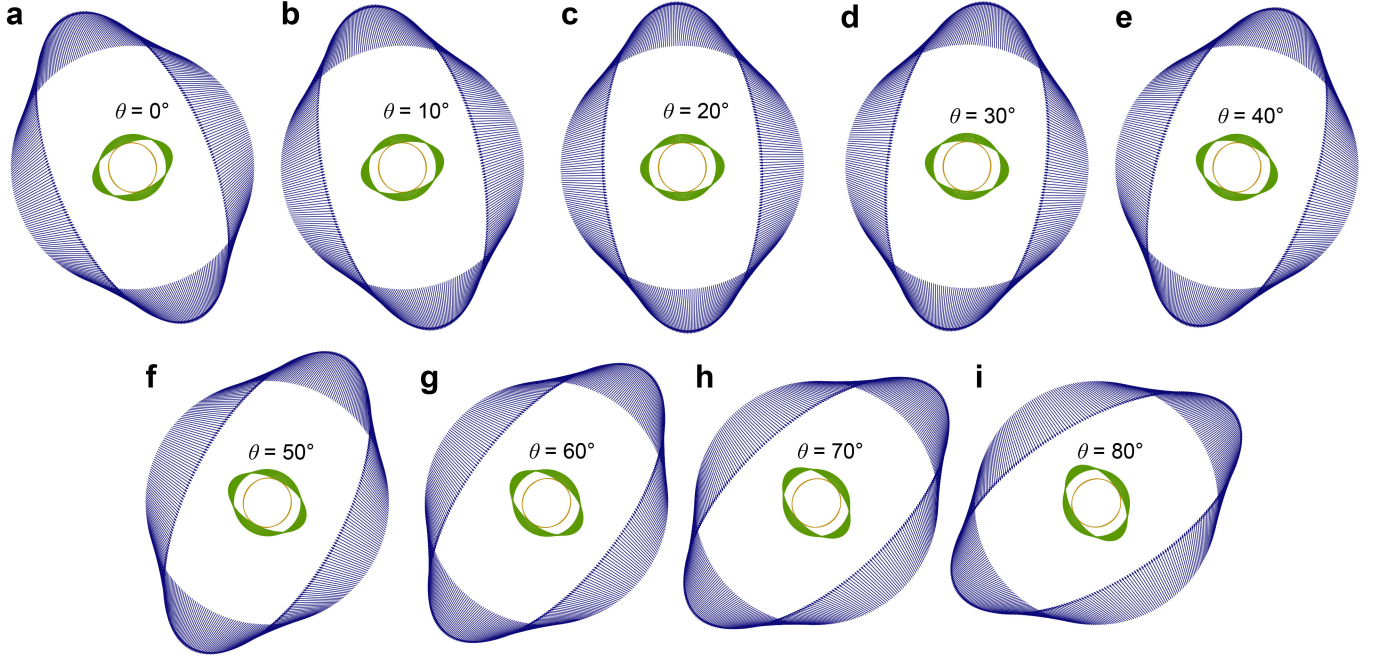


FIG. A2. The distribution of the force density vector with an azimuthal resolution of  $1^\circ$ . Subfigures correspond to different polarization angles ( $\theta = 10^\circ, 20^\circ, \dots, 80^\circ$ ) for the GW source.

power over an isotropic, stochastic background of GWs. This ‘‘polarization average,’’ denoted by  $\langle \dots \rangle_{\text{pol}}$ , corresponds to an integral over all possible propagation directions and polarizations. For a quantity  $X(e, \lambda, \nu)$  that depends on the GW parameters, the average is defined as:

$$\langle X \rangle_{\text{pol}} \equiv \frac{1}{4\pi} \int_0^{2\pi} d\lambda \int_0^\pi d\epsilon \sin \epsilon \left[ \frac{1}{2\pi} \int_0^{2\pi} d\nu X \right]. \quad (\text{A11})$$

The inner integral averages over the polarization angle  $\nu$ , while the outer integrals average over the celestial sphere (all propagation directions). For 2D SEM simulation, the average is simplified to

$$\langle X \rangle_{\text{pol,SEM}} \equiv \frac{1}{n+1} \sum_{i=0}^n X(\theta_i) \quad (\text{A12})$$

This procedure is applied to both the numerator and the denominator in Eq. (6) and Eq. (7) of the main text to compute the energy magnification factors  $m_E$  and  $M_E$ .

## F. Woodhouse Kernels

The elements of the coupling matrices,  $V_{kk'} = \langle k | \delta \mathcal{V} | k' \rangle$  and  $T_{kk'} = \langle k | \delta \mathcal{T} | k' \rangle$ , are volume integrals of the structural perturbations multiplied by the unperturbed eigenfunctions. The formalism developed by Woodhouse provides an elegant and efficient method for computing these integrals. In the actual calculations of this work, we mainly apply the detailed and clear formalism presented in *Theoretical Global Seismology* [30],

except for correcting a small typo in Eq. (D.160) of the book:

$$M_{kk'}^{m0} = -\sqrt{2} \text{Im } \tilde{M}_{kk'}^{m0}. \quad (\text{A13})$$

We also omit all parts related to gravity potential perturbation, for simplicity.

In general, in the case of our perturbation model, the coupling matrix elements (in complex basis, following the form of the reference) are calculated as

$$\begin{aligned} (\tilde{\mathbf{T}}^{k'k})_{m_1 m_2} = & \sum_{st} (-1)^{m_1} \left[ \frac{(2l+1)(2s+1)(2l'+1)}{4\pi} \right]^{1/2} \\ & \times \begin{pmatrix} l & s & l' \\ -m_1 & t & m_2 \end{pmatrix} \\ & \times \left\{ \int_0^R \delta \tilde{\rho}_{st} T_\rho r^2 dr + \sum_d d^2 \delta \tilde{d}_{st} [T_d]^\dagger \right\} \end{aligned} \quad (\text{A14})$$

$$\begin{aligned} (\tilde{\mathbf{V}}^{k'k})_{m_1 m_2} = & \sum_{st} (-1)^{m_1} \left[ \frac{(2l+1)(2s+1)(2l'+1)}{4\pi} \right]^{1/2} \\ & \times \begin{pmatrix} l & s & l' \\ -m_1 & t & m_2 \end{pmatrix} \\ & \times \left\{ \int_0^R \delta \tilde{\rho}_{st} V_\rho r^2 dr + \sum_d d^2 \delta \tilde{d}_{st} [V_d]^\dagger \right\} \end{aligned} \quad (\text{A15})$$

In these formulae, all the structural perturbations (e.g., density  $\delta \rho$ , boundary  $\delta d$ ) are expanded in complex spherical harmonics. For example:

$$\delta \rho(\vec{r}) = \sum_{s,t} \delta \tilde{\rho}_{st}(r) Y_{st}(\theta, \phi). \quad (\text{A16})$$

The core of the method is to separate the volume integral into radial and angular parts.

The angular integrals involve products of three spherical harmonics (one from each of the two eigenfunctions and one from the perturbation) and can be calculated analytically using Gaunt integrals or, more generally, Wigner 3-j symbols. These symbols enforce strict selection rules on the angular orders, e.g.,  $|l - l'| \leq s \leq l + l'$ .

The remaining radial integral is expressed in terms of “**Woodhouse kernels**.” These kernels, such as  $V_\rho$ ,  $V_d$ ,  $T_\rho$ ,  $T_d$ , are functions of radius that depend only on the radial eigenfunctions of the two modes being coupled ( $|k\rangle$  and  $|k'\rangle$ ). They represent the sensitivity of the coupling interaction to a structural anomaly at a given depth. For example, for spheroidal-spheroidal (SS) coupling, the kinetic kernel  $T_\rho^{SS}$  has a simple form:

$$T_{\rho, kk'}^{SS}(r) = U_k(r)U_{k'}(r)B_{lsl'}^{(0)+} + V_k(r)V_{k'}(r)B_{lsl'}^{(1)+}, \quad (A17)$$

where  $U, V$  are the radial eigenfunctions and the  $B$  coefficients contain the Wigner 3-j symbols that handle the angular geometry. This semi-analytic approach is computationally more efficient than a direct 3D numerical integration.

#### G. Amplification $m_E(\omega)$ from mode-coupling calculation

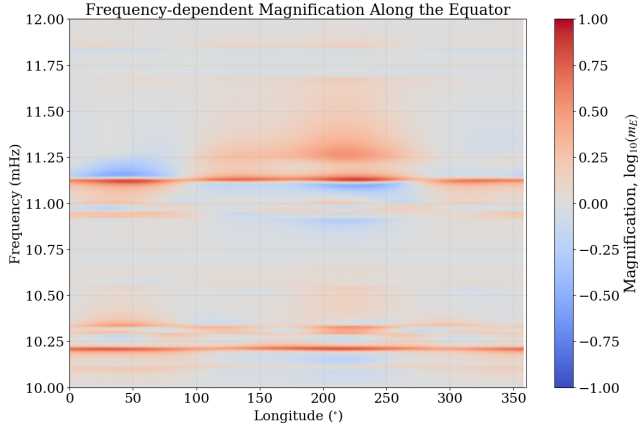


FIG. A3. Frequency-dependent magnification factor  $m_E(\vec{r}, \omega)$  along the lunar equator. The thicker crust (around  $200^\circ - 250^\circ$ ) shows systematically higher amplification across a wide frequency band.

Figure A3 displays the frequency-dependent amplification factor  $m_E(\vec{r}, \omega)$  derived from our analytical mode-coupling framework. Unlike the SEM results presented in the main text (Figure 2f), which follow a great circle traversing the SPA basin and Mare Imbrium, this profile calculates the response along the lunar equator. Furthermore, the calculation focuses on a representative frequency window (10–12 mHz) to illustrate the modal response details. Despite the differences in the selected path and numerical method, the physical pattern remains consistent with our main findings: signal amplification shows a clear positive correlation with crustal structure. For example, we can see that the equatorial region characterized by thicker crust (approximately  $200^\circ - 250^\circ$ ) consistently exhibits higher magnification levels, corroborating the robust link between crustal thickness and GW signal enhancement.